Research Square

Preprints are preliminary reports that have not undergone peer review.
They should not be considered conclusive, used to inform clinical practice,
or referenced by the media as validated information.

Worst-case Analysis for Fixed-wing Aircraft Automated Landing based on Counter Optimization

Yuanyuan Hao
Shanghai Jiao Tong University
Xuanyu Chen
Shanghai Jiao Tong University
Shen Kang
Beijing Galactic Energy Space Technology Co., Ltd.
Florian Holzapfel
Technische Universität München
Haichao Hong
haichao.hong@sjtu.edu.cn
Shanghai Jiao Tong University
Shiqiang Hu
Shanghai Jiao Tong University

Research Article

Keywords:

Posted Date: November 10th, 2026

DOI: https://doi.org/10.21203/rs.3.rs-9374356/v1

License: This work is licensed under a Creative Commons Attribution 4.0 International License.
Read Full License

Additional Declarations: No competing interests reported.

Worst-case Analysis for Fixed-wing Aircraft Automated Landing based on Counter Optimization

Yuanyuan Hao[1], Xuanyu Chen[1], Shen Kang[2], Florian Holzapfel[3], Haichao Hong[1,*], Shiqiang Hu[1]

1 School of Aeronautics and Astronautics, Shanghai Jiao Tong University, Shanghai 200240, China
2 Beijing Galactic Energy Space Technology Co., Ltd., CATIC Plaza, Yizhuang, Beijing, China
3 Institute of Flight System Dynamics, Technische Universität München, Boltzmannstraße 15, Garching D-85748, Germany
* Corresponding Author

Abstract. Automated landing of fixed-wing aircraft is inevitably affected by wind disturbances. The evaluation of operational safety is often performed using Monte Carlo methods, yet they are inefficient at identifying the worst-case scenario rendering the resulting performance boundaries unreliable. To this end, this work directly identifies the worst-case wind disturbance against the safe landing based on counter optimization. Specifically, the three-dimensional wind disturbance is treated as the decision variable to maximize a set of error metrics that quantify landing performance. These metrics include lateral deviation, longitudinal deviation, airspeed error, and touchdown sink rate. Maximizing each metric formulates an optimization problem that is solved using Particle Swarm Optimization (PSO). The worst-case wind profile for each metric is identified for a given landing reference trajectory. A comprehensive understanding of the performance boundaries is therefore formed.

Keywords: counter optimization, fixed-wing aircraft, automated landing, worst-case wind disturbance, particle swarm optimization, flight control evaluation

1 Introduction

This paper applies counter optimization to evaluate the landing performance of a fixed-wing aircraft autopilot under wind disturbances. Rather than randomly sampling wind as in conventional Monte Carlo methods, counter optimization searches within physically realistic bounds for the three-dimensional wind disturbance history that maximizes touchdown error. The resulting worst-case scenario reveals which control channel is the most vulnerable and under what flight conditions.

This work focuses on landing because landing is the most critical phase of the flight. Boeing's long-term statistics [1] show that final approach and landing

account for approximately 4% of total flight time yet are involved in nearly half of all fatal accidents. Small fixed-wing aircraft exhibit high sensitivity to wind disturbances. Light weight and low approach speeds lead to control surface saturation under crosswind gusts [2]. Deceleration on the glide slope reduces dynamic pressure and control effectiveness, amplifying the sensitivity to wind disturbances.

A large body of work addresses controller design for aircraft landing in wind, including disturbance-observer-based control [3], dynamic inversion with backstepping [4], incremental nonlinear dynamic inversion (INDI) [5] and incremental sliding-mode control [6], wind-compensated path following [7], and active-disturbance-rejection control tested in flight [8]. These studies test their controllers using a similar approach. Performance is evaluated under Dryden or von Kármán stochastic wind models. Average tracking error across random runs serves as the performance metric. Monte Carlo simulation serves as the standard tool. Yin et al. [9] used it for probabilistic flight envelope estimation, and Lu et al. [10] proposed optimal-control-based reachability to reduce computation. However, in this work, wind disturbance during landing constitutes a high-dimensional time series. Within this high-dimensional space, Monte Carlo simulation effectively estimates mean values but exhibits low efficiency in worst-case identification.

Counter optimization maximizes the error cost function under physical constraints. The idea originates from flight control law clearance [11], where Diepolder [12] built an optimal-control-based framework later packaged as the COLIBRY toolbox [13]. Braun et al. [14] applied deep Q-learning to find worst-case inputs for eVTOL envelope protections and extended the approach to fly-by-wire flight control law testing [15]. More recently, the same group incorporated reinforcement learning to handle complex constraints [16]. Counter optimization provides a directed search within the disturbance space. This method identifies critical regions and generates interpretable worst-case scenarios, contrasting with the pass/fail statistics of Monte Carlo simulations.

In this work, we propose to assess the landing performance of an automated landing with an L_1 guidance law and a TECS-based longitudinal controller under wind disturbance through counter optimization. The wind disturbance is selected as the decision variable to maximize error metrics that are commonly used to evaluate the landing performance. Four landing metrics are used, namely, lateral deviation, longitudinal deviation, airspeed error, and touchdown sink rate. Each metric is optimized independently using Particle Swarm Optimization (PSO). The objective of this work is to evaluate the existing controllers rather than design new ones. Identified worst-case disturbances generates more reliable performance boundaries, and therefore reveal critical flight conditions.

The remainder of the paper is organized as follows. Section 2 describes the 6-DOF aircraft model and autopilot. Section 3 formulates the counter optimization problem. Section 4 presents and analyzes the simulation results, and Section 5 concludes the paper.

2 Aircraft Dynamics and Autopilot

2.1 Six-Degree-of-Freedom Aircraft Dynamics

The fixed-wing aircraft is modeled as a rigid body with six degrees of freedom. Its state vector is

$$\mathbf{x} = \left[\, p_n,\ p_e,\ p_d,\ \phi,\ \theta,\ \psi,\ u,\ v,\ w,\ p,\ q,\ r \,\right]^\top, \tag{1}$$

where (p_n, p_e, p_d) is the position in the North-East-Down (NED) frame, (ϕ, θ, ψ) denotes the Euler angles, (u, v, w) are the body-axis velocity components, and (p, q, r) are the angular rates about the body axes.

In the body frame, the translational dynamics read

$$m\left(\dot{\mathbf{V}}_b + \boldsymbol{\omega}_b \times \mathbf{V}_b\right) = \mathbf{F}_b, \tag{2}$$

with $\mathbf{V}_b = [u,\, v,\, w]^\top$, $\boldsymbol{\omega}_b = [p,\, q,\, r]^\top$, and $\mathbf{F}_b = [F_x,\, F_y,\, F_z]^\top$. Expanding (2) yields

$$\begin{bmatrix} \dot{u} \\ \dot{v} \\ \dot{w} \end{bmatrix} = \begin{bmatrix} rv - qw \\ pw - ru \\ qu - pv \end{bmatrix} + \frac{1}{m}\begin{bmatrix} F_x \\ F_y \\ F_z \end{bmatrix}. \tag{3}$$

The total external force is the sum of three terms:

$$\mathbf{F}_b = \mathbf{F}_A + \mathbf{F}_T + \mathbf{F}_g, \tag{4}$$

namely the aerodynamic force $\mathbf{F}_A$, the thrust force $\mathbf{F}_T = [T,\, 0,\, 0]^\top$ (assumed along the body x-axis), and the gravitational force expressed in the body frame:

$$\mathbf{F}_g = m\mathbf{R}^\top(\boldsymbol{\Phi}) \begin{bmatrix} 0 \\ 0 \\ g \end{bmatrix}, \tag{5}$$

where g is the gravitational acceleration and $\mathbf{R}(\boldsymbol{\Phi})$ is the direction-cosine matrix from the body frame to the NED frame.

The rotational dynamics obey Euler's rigid-body equation:

$$\mathbf{J}\dot{\boldsymbol{\omega}}_b + \boldsymbol{\omega}_b \times (\mathbf{J}\boldsymbol{\omega}_b) = \mathbf{M}_b, \tag{6}$$

where $\mathbf{J}$ is the inertia matrix and $\mathbf{M}_b = [L,\, M,\, N]^\top$ is the total external moment in the body frame. This can be rewritten as

$$\begin{bmatrix} \dot{p} \\ \dot{q} \\ \dot{r} \end{bmatrix} = \mathbf{J}^{-1}\left(\begin{bmatrix} L \\ M \\ N \end{bmatrix} - \begin{bmatrix} p \\ q \\ r \end{bmatrix} \times \mathbf{J}\begin{bmatrix} p \\ q \\ r \end{bmatrix}\right). \tag{7}$$

The total moment has an aerodynamic part and a thrust-induced part: $\mathbf{M}_b = \mathbf{M}_A + \mathbf{M}_T$.

Both the aerodynamic force and moment are computed from the air-relative velocity. With airspeed magnitude V_a, the dynamic pressure is $\bar{q} = \frac{1}{2}\rho V_a^2$, and the aerodynamic force and moment take the form

$$\mathbf{F}_A = \bar{q}\, S \begin{bmatrix} C_X \\ C_Y \\ C_Z \end{bmatrix}, \qquad \mathbf{M}_A = \bar{q}\, S \begin{bmatrix} bC_l \\ \bar{c}C_m \\ bC_n \end{bmatrix}, \tag{8}$$

where S is the reference wing area, b the wingspan, $\bar{c}$ the mean aerodynamic chord, and C_X, C_Y, C_Z and C_l, C_m, C_n are the body-axis force and moment coefficients, respectively. These coefficients depend on the angle of attack α, the sideslip angle β, the angular rates, and the control inputs $\boldsymbol{\delta} = [\delta_e,\, \delta_a,\, \delta_r,\, \delta_t]^\top$ (elevator, aileron, rudder, and throttle).

Position propagation in the NED frame follows

$$\begin{bmatrix} \dot{p}_n \\ \dot{p}_e \\ \dot{p}_d \end{bmatrix} = \mathbf{R}(\boldsymbol{\Phi}) \begin{bmatrix} u \\ v \\ w \end{bmatrix}, \tag{9}$$

and the Euler-angle rates are related to the body angular rates by

$$\begin{bmatrix} \dot{\phi} \\ \dot{\theta} \\ \dot{\psi} \end{bmatrix} = \begin{bmatrix} 1 & s_\phi t_\theta & c_\phi t_\theta \\ 0 & c_\phi & -s_\phi \\ 0 & s_\phi/c_\theta & c_\phi/c_\theta \end{bmatrix} \begin{bmatrix} p \\ q \\ r \end{bmatrix}, \tag{10}$$

where $c_{(\cdot)} := \cos(\cdot)$, $s_{(\cdot)} := \sin(\cdot)$, $t_{(\cdot)} := \tan(\cdot)$. The direction-cosine matrix is

$$\mathbf{R} = \begin{bmatrix} c_\theta c_\psi & s_\phi s_\theta c_\psi - c_\phi s_\psi & c_\phi s_\theta c_\psi + s_\phi s_\psi \\ c_\theta s_\psi & s_\phi s_\theta s_\psi + c_\phi c_\psi & c_\phi s_\theta s_\psi - s_\phi c_\psi \\ -s_\theta & s_\phi c_\theta & c_\phi c_\theta \end{bmatrix}. \tag{11}$$

The time-varying wind velocity in the NED frame is denoted

$$\mathbf{V}_w^n(t) = \begin{bmatrix} W_n(t) \\ W_e(t) \\ W_d(t) \end{bmatrix}. \tag{12}$$

Rotating this vector into the body frame, $\mathbf{V}_w^b = \mathbf{R}^\top \mathbf{V}_w^n$, gives the air-relative velocity

$$\mathbf{V}_r = \begin{bmatrix} u_r \\ v_r \\ w_r \end{bmatrix} = \begin{bmatrix} u \\ v \\ w \end{bmatrix} - \mathbf{V}_w^b, \tag{13}$$

from which the standard aerodynamic quantities follow:

$$V_a = \sqrt{u_r^2 + v_r^2 + w_r^2}, \qquad \alpha = \arctan\!\left(\frac{w_r}{u_r}\right), \qquad \beta = \arcsin\!\left(\frac{v_r}{V_a}\right). \tag{14}$$

The wind disturbance enters the dynamics by altering the air-relative velocity, which in turn modifies V_a, α, and β and therefore both the aerodynamic force and moment. In this work, the wind $\mathbf{V}_w^n(t)$ is not treated as a random process but as the decision variable of the counter optimization problem introduced in Section 3.

2.2 Autopilot and Guidance

The landing autopilot uses a cascaded architecture with an outer guidance loop and inner attitude and rate control loops.

Lateral path tracking employs the L_1 nonlinear guidance law. Given the current aircraft position $\mathbf{p} = [p_n,\, p_e]^\top$ and the straight-line segment from waypoint $\mathbf{w}_{k-1}$ to $\mathbf{w}_k$, the commanded course angle is

$$\chi_c = \chi_L + \arcsin\left(\frac{2\, d_\perp\, V_g^2}{L_1^2\, g}\right), \tag{15}$$

where χ_L is the line-of-sight angle to a reference point on the path at distance L_1 ahead of the aircraft, $d_\perp$ is the cross-track error, and V_g is the ground speed. The look-ahead distance is fixed at $L_1 = 50$ m throughout the approach.

Altitude and airspeed commands are obtained by linear interpolation along the current path segment. Let $\hat{\mathbf{e}} = (\mathbf{w}_k - \mathbf{w}_{k-1})/\|\mathbf{w}_k - \mathbf{w}_{k-1}\|$ denote the unit direction vector of the segment. With the progress fraction defined as

$$\eta = \mathrm{clamp}\left(\frac{(\mathbf{p} - \mathbf{w}_{k-1})^\top \hat{\mathbf{e}}}{\|\mathbf{w}_k - \mathbf{w}_{k-1}\|},\ 0,\ 1\right), \tag{16}$$

the references become

$$h_c = h_{k-1} + \eta\,(h_k - h_{k-1}), \qquad V_{a,c} = V_{a,k-1} + \eta\,(V_{a,k} - V_{a,k-1}), \tag{17}$$

where h_k and $V_{a,k}$ are the altitude and airspeed assigned at waypoint k.

Roll and pitch angles are regulated by PID controllers that output aileron and elevator commands, respectively. Yaw coordination is achieved through a sideslip-feedback rudder controller. Throttle is managed by an algorithm based on the total-energy-control system (TECS), which balances altitude and airspeed errors simultaneously. All actuator commands are subject to saturation limits.

The guidance logic advances to the next segment once the aircraft enters a capture radius of $r_{\mathrm{wp}} = 35$ m around the current target waypoint. Twelve waypoints define the straight-in landing trajectory. The altitude decreases from 100 m to 2 m. Airspeed reduces from 25 m/s to 19.5 m/s during this descent.

3 Counter Optimization Problem Setup

The wind disturbance is treated as the decision variable of an optimization problem. For each of the four landing metrics, the problem reads

$$\mathbf{z}_k^* = \arg\max_{\mathbf{z}\in\mathcal{Z}} J_k\big(\mathbf{x}(t_f;\mathbf{z})\big), \qquad k = 1,\ldots,4, \tag{18}$$

where $\mathcal{Z}$ is the admissible set of discretized disturbance vectors, $\mathbf{z}$ is the decision variable collecting the disturbance values at the control points, and J_k is one of four landing metrics evaluated at touchdown time t_f. The continuous wind disturbance $\mathbf{V}_w^n(t)$ is reconstructed from $\mathbf{z}$ via piecewise cubic Hermite interpolation. Each metric is optimized in a separate PSO run, yielding four distinct worst-case wind profiles.

3.1 Wind Disturbance Model

Optimizing a continuous disturbance waveform over the full mission horizon $[0, T]$ directly is impractical. The wind is therefore discretized at N_c equally spaced control points separated by Δt_w. For the landing scenario considered in this work, $T = 120$ s and $\Delta t_w = 12$ s, giving

$$N_c = \left\lfloor \frac{T}{\Delta t_w} \right\rfloor + 1 = 11. \tag{19}$$

At each control point $j \in \{1, \ldots, N_c\}$, three NED disturbance components are specified. Stacking them into a single vector yields

$$\mathbf{z} = \big[\underbrace{W_n^{(1)}, \ldots, W_n^{(N_c)}}_{\text{north}}, \underbrace{W_e^{(1)}, \ldots, W_e^{(N_c)}}_{\text{east}}, \underbrace{W_d^{(1)}, \ldots, W_d^{(N_c)}}_{\text{down}} \big]^\top \in \mathbb{R}^{3N_c}, \tag{20}$$

so the total number of decision variables is $n_{\text{var}} = 3N_c = 33$.

Between control points, the disturbance is reconstructed by piecewise cubic Hermite interpolation (PCHIP):

$$W_i(t) = \text{pchip}\Big(\{t_j\}_{j=1}^{N_c}, \{W_i^{(j)}\}_{j=1}^{N_c}; t \Big), \qquad i \in \{n, e, d\}. \tag{21}$$

PCHIP produces a smooth time history while avoiding the overshoots that can occur with unconstrained cubic splines.

Several constraints are imposed to keep the optimized disturbance physically plausible. Each disturbance component is bounded as

$$W_n^{(j)},\ W_e^{(j)} \in [-6,\ 6] \text{ m/s}, \qquad W_d^{(j)} \in [-1.5,\ 1.5] \text{ m/s}, \tag{22}$$

for all $j = 1, \ldots, N_c$. The horizontal bound of 6 m/s corresponds to the moderate and strong wind envelope. The vertical bound is set to one quarter of the horizontal value, because sustained vertical gusts are typically weaker than horizontal winds.

The rate of change between adjacent control points is limited by

$$\frac{|W_i^{(j)} - W_i^{(j-1)}|}{\Delta t_w} \le \dot{W}_{\max}, \qquad j = 2, \ldots, N_c, \quad i \in \{n, e\}, \tag{23}$$

with $\dot{W}_{\max} = 0.5$ m/s^2. A tighter limit is applied to the vertical component:

$$\frac{|W_d^{(j)} - W_d^{(j-1)}|}{\Delta t_w} \le \dot{W}_{d,\max}, \qquad j = 2, \ldots, N_c, \tag{24}$$

where $\dot{W}_{d,\max} = \kappa_d \dot{W}_{\max}$ with $\kappa_d = 0.3$.

A second-order finite-difference constraint prevents unrealistic oscillations:

$$\frac{\left|\Delta W_i^{(j)} - \Delta W_i^{(j-1)}\right|}{\Delta t_w^2} \le \ddot{W}_{\max}, \qquad j = 3, \ldots, N_c, \tag{25}$$

where $\Delta W_i^{(j)} := W_i^{(j)} - W_i^{(j-1)}$ and $\ddot{W}_{\max} = 0.04$ m/s^3. Because PCHIP interpolation is only C^1-continuous, the true second derivative of the reconstructed wind may still jump at the control-point knots. The constraint (25) limits the discrete second-order difference at these knots but does not enforce continuity of the second derivative between them. Discontinuities remain minimal. The first-order rate constraint (23) restricts the slope change between adjacent intervals.

The root-mean-square magnitude of the horizontal disturbance is constrained to avoid saturation at the upper bounds. This work implements the following cap:

$$W_{\text{rms}} := \sqrt{\frac{1}{N_c}\sum_{j=1}^{N_c}\left[\left(W_n^{(j)}\right)^2 + \left(W_e^{(j)}\right)^2\right]} \le W_{\text{rms,max}}, \tag{26}$$

with $W_{\text{rms,max}} = 4.0$ m/s.

A projection step enforces amplitude, rate, smoothness, and RMS constraints before each simulation call. This procedure ensures the feasibility of all evaluated candidates.

3.2 Objective Function

The objective quantifies how much the optimized wind degrades landing performance relative to the commanded references. Four terminal metrics are defined at the touchdown time:

$$\begin{aligned} J_1 &= |y(t_f)|\,, \\ J_2 &= |x(t_f) - x_{\text{ref}}(t_f)|\,, \\ J_3 &= |V(t_f) - V_{\text{ref}}(t_f)|\,, \\ J_4 &= V(t_f)\cdot \sin\gamma(t_f). \end{aligned} \tag{27}$$

Each metric is used as a standalone objective in a separate optimization run. The PSO minimizes

$$f_k(\mathbf{z}) = \begin{cases} -\left(J_k - P_{\text{wind}}\right), & \text{if the simulation is non-divergent,} \\ C_\infty, & \text{otherwise,} \end{cases} \tag{28}$$

where $C_\infty = 10^4$ is a large penalty constant. The negative sign converts the maximization of landing degradation into a minimization problem suitable for PSO.

Each metric has different units and scales. Running four independent optimizations avoids the need for normalization constants and weight coefficients. The worst-case wind for each channel is identified separately.

A simulation is classified as divergent and assigned cost C_∞ if the airspeed drops below $V_{a,\text{div}} = 10$ m/s or the simulation completes less than 50% of the mission horizon.

A regularization term P_{wind} penalizes constraint violations to encourage smooth disturbance histories:

$$P_{\text{wind}} = \lambda_r \sum_{j=2}^{N_c} \max\Big(0,\ \Big|\dot{W}_n^{(j)}\Big| - \dot{W}_{\max}\Big)^2 + \lambda_{\text{rms}} \max(0,\ W_{\text{rms}} - W_{\text{rms,max}})^2\,, \tag{29}$$

with $\lambda_r = 5$ and $\lambda_{\text{rms}} = 10$.

Flight-envelope quantities such as peak angle of attack, peak roll angle, minimum airspeed, and peak sink rate are recorded during each simulation for post-optimization inspection.

3.3 Solution Method

Each of the four optimization problems is solved with Particle Swarm Optimization (PSO) using $N_p = 200$ particles and up to 600 iterations. The objective landscape is non-smooth and non-differentiable due to nonlinear 6-DOF dynamics. This work employs PSO to handle these gradient free characteristics.

To speed up convergence, the initial swarm includes several structured disturbance patterns alongside random samples:

1. *Rotating disturbance* (20% of particles): Constant magnitude with slowly varying direction. This category models sustained crosswinds.
2. *Ramping disturbance with downdraft* (20%): a magnitude that grows over time, combined with a persistent downward component.
3. *Shear-like disturbance* (15%): a rapid transition between opposing horizontal directions.
4. *Late-stage crosswind* (20%): a stronger lateral disturbance concentrated in the final approach phase, with a localized downward component.
5. *Direction-reversal disturbance* (15%): a weak early disturbance followed by a stronger one from a different direction.
6. *Random smooth disturbance* (10%): low pass filtered random samples that maintain population diversity.

The same initial swarm is used for all four optimization runs. The cognitive and social coefficients are both set to $c_1 = c_2 = 1.49$. The minimum neighborhood fraction is 0.15, and the function tolerance for convergence is 10^{-4}. All simulation evaluations are parallelized across the available CPU cores.

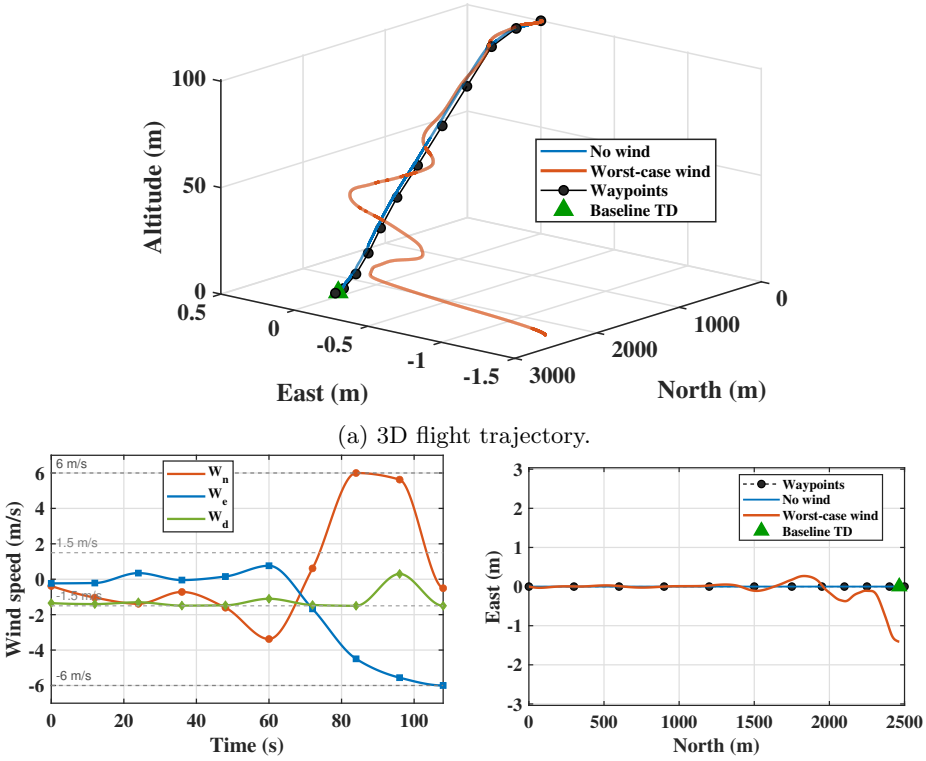
4 Results and Discussion

4.1 Simulation Setup

The landing scenario spans $T = 120$ s. The landing approach follows a 12-waypoint straight trajectory. Initial altitude is $h_0 = 100$ m, with touchdown at $h_{\text{td}} = 2$ m. The commanded airspeed decreases from 25 m/s to 19.5 m/s along the approach. The integration step is $\Delta t = 0.01$ s.

The wind is discretized at $N_c = 11$ equally spaced control points ($\Delta t_w = 12$ s), giving $n_{\text{var}} = 33$ decision variables. Continuous wind histories are reconstructed by PCHIP interpolation. The PSO solver uses $N_p = 200$ particles and at most 600 iterations. All fitness evaluations are parallelized across available CPU cores. The initial swarm contains six structured seed patterns and uniformly sampled candidates. The same initial population is used for all four optimization runs.

A zero-wind baseline simulation yields the touchdown state $p_n^0 = 2465$ m, $p_e^0 = 0$ m, $V_a^0 = 20.9$ m/s, $\dot{h}^0 = 0.48$ m/s. This trajectory is retained for comparison in the figures. Δy and Δx are measured relative to the waypoint path. ΔV_a is measured relative to the commanded schedule. The approach path follows the northward direction. A positive northward wind component $W_n > 0$ denotes a tailwind. Positive components W_e and W_d denote eastward and downward wind, respectively.

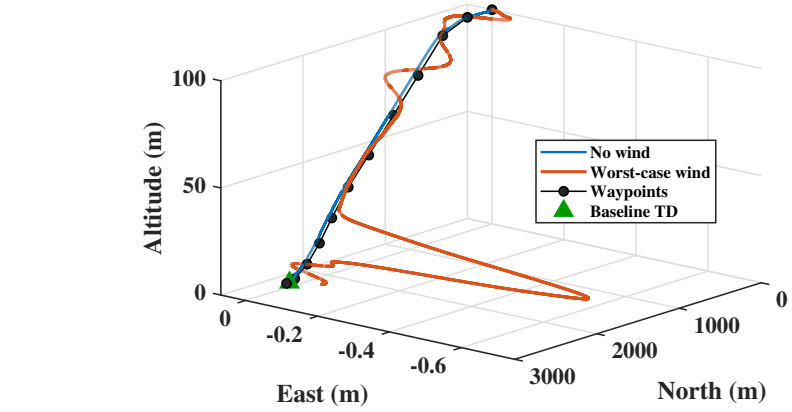


(a) 3D flight trajectory.

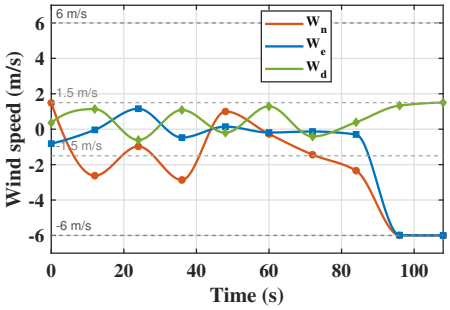
(b) Wind NED components.

(c) Horizontal trajectory.

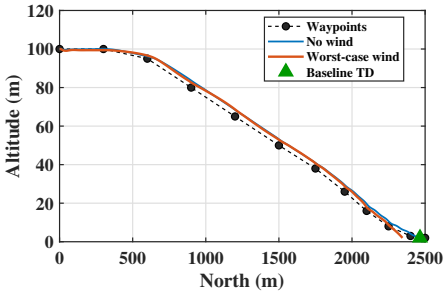
Fig. 1: Worst-case wind and trajectory for lateral deviation.



(a) 3D flight trajectory.



(b) Wind NED components.



(c) Longitudinal profile.

Fig. 2: Worst-case wind and trajectory for longitudinal deviation.

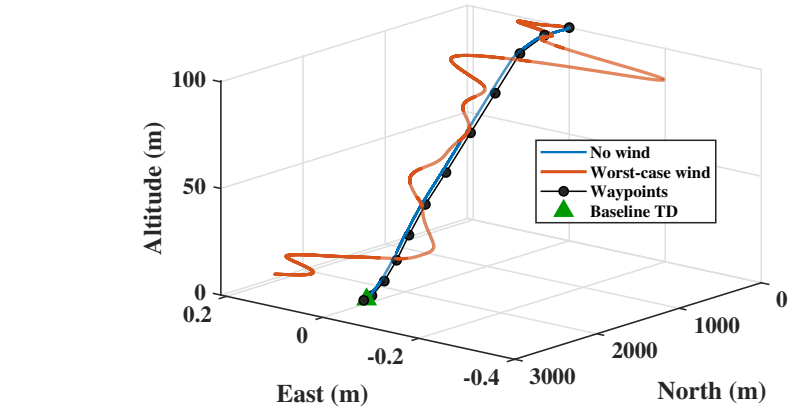
4.2 Optimization Results

Each of the four landing metrics is maximized in a separate PSO run. The results are presented in the order of lateral deviation, longitudinal deviation, airspeed error, and touchdown sink rate.

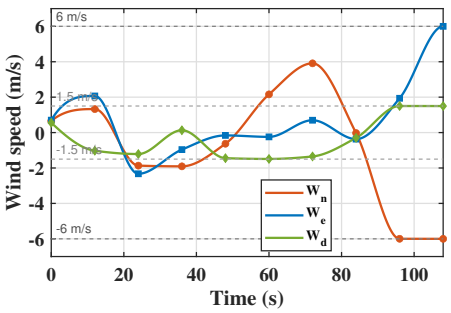
Fig. 1(b) shows the worst-case wind for lateral deviation Δy. For W_n and W_e, the initial 60 s interval is characterized by low-amplitude oscillations. At $t = 84$ s, W_n rises to 6 m/s, reaching the upper bound. W_e decreases to -4.5 m/s at $t = 84$ s and -6 m/s at $t = 108$ s. W_d stays near -1.5 m/s throughout the approach, with a brief excursion to $+0.3$ m/s at $t = 96$ s.

The worst-case tailwind and crosswind are concentrated in the final approach segment. The tailwind increases ground speed, while the westward crosswind $W_e < 0$ induces lateral aerodynamic forces. These disturbances occur below 30 m altitude, coinciding with minimum dynamic pressure and reduced roll authority.

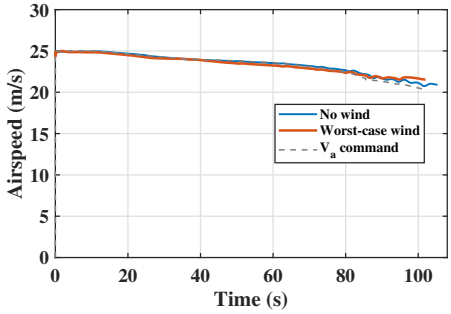
The trajectory (Fig. 1(a, c)) tracks the baseline above 30 m. Below 30 m, the trajectory drifts westward. The cross-track error peaks near $p_n \approx 2300$ m. The resulting cross-track deviation is $\Delta y = 1.41$ m.



(a) 3D flight trajectory.



(b) Wind NED components.



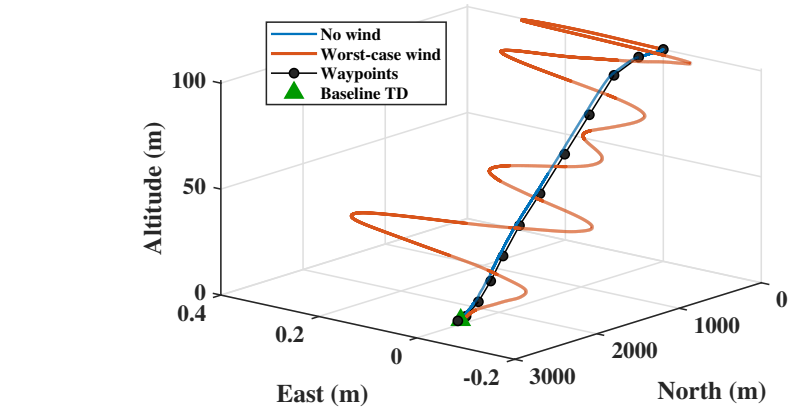
(c) Airspeed time history.

Fig. 3: Worst-case wind and trajectory for airspeed error.

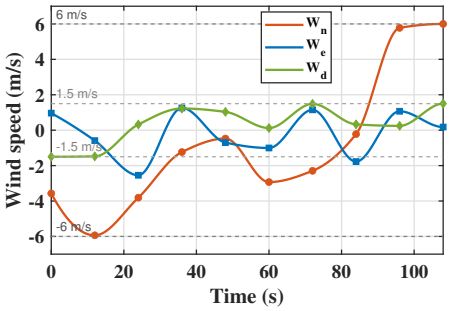
Fig. 2(b) shows the worst-case wind for longitudinal deviation Δx. After $t > 84$ s, the three-axis wind components saturate the constraint bounds. The resulting headwind reduces the ground speed while the TECS controller maintains the commanded airspeed and glide slope. The altitude profile (Fig. 2(c)) shows that the descent path follows the planned waypoints throughout the approach. The aircraft reaches the 2 m altitude threshold 155 m before the target waypoint. The simulation terminates at this point.

Fig. 3(b) shows structural similarity to the longitudinal case, with peak disturbance magnitudes concentrated in the final approach segment. Fig. 3(c) shows the airspeed response. The airspeed follows the command from 25 m/s to approximately 22 m/s during the first 80 s. In the final segment, the airspeed rises above the command. The airspeed error at touchdown is $\Delta V_a = 2.02$ m/s.

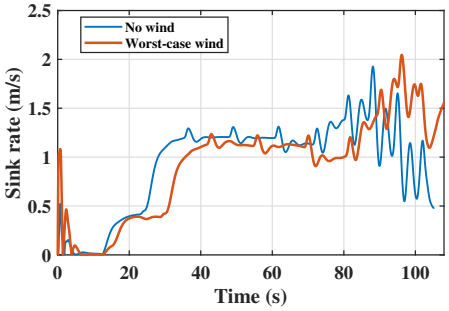
The worst-case wind for $\dot{h}_{\text{td}}$ (Fig. 4(b)) exhibits an oscillatory structure. The sink rate history (Fig. 4(c)) reflects the effect of this wind profile. The initial updraft maintains the sink rate below the baseline for $t \in [20, 90]$ s. Subsequently, the coupled tailwind reversal and downdraft induce sink rate divergence, peaking



(a) 3D flight trajectory.



(b) Wind NED components.



(c) Sink rate time history.

Fig. 4: Worst-case wind and trajectory for touchdown sink rate.

at 2.05 m/s near $t = 95$ s. The resulting touchdown sink rate is $\dot{h}_{\text{td}} = 1.60$ m/s, a 233% increase relative to the 0.48 m/s baseline.

4.3 Comparison and Discussion

Table 1 collects all four landing metrics for each optimization run. Each row corresponds to one PSO run. The bold entry is the targeted metric. The remaining columns report the other three metrics under the same worst-case wind. Fig. 5 overlays the NED components of the four worst-case wind profiles.

The following observations are drawn from Table 1 and Fig. 5.

1. All four optimized wind profiles concentrate their energy below 40 m altitude. In this region, W_n and W_e reach the ± 6 m/s bounds. This is because the dynamic pressure is lowest during the final approach. The control authority is reduced accordingly. Fig. 5 confirms this pattern across all four runs.
2. The vertical component W_d shows the highest variability among the four runs. This is because W_d affects each metric through a different physical path. It

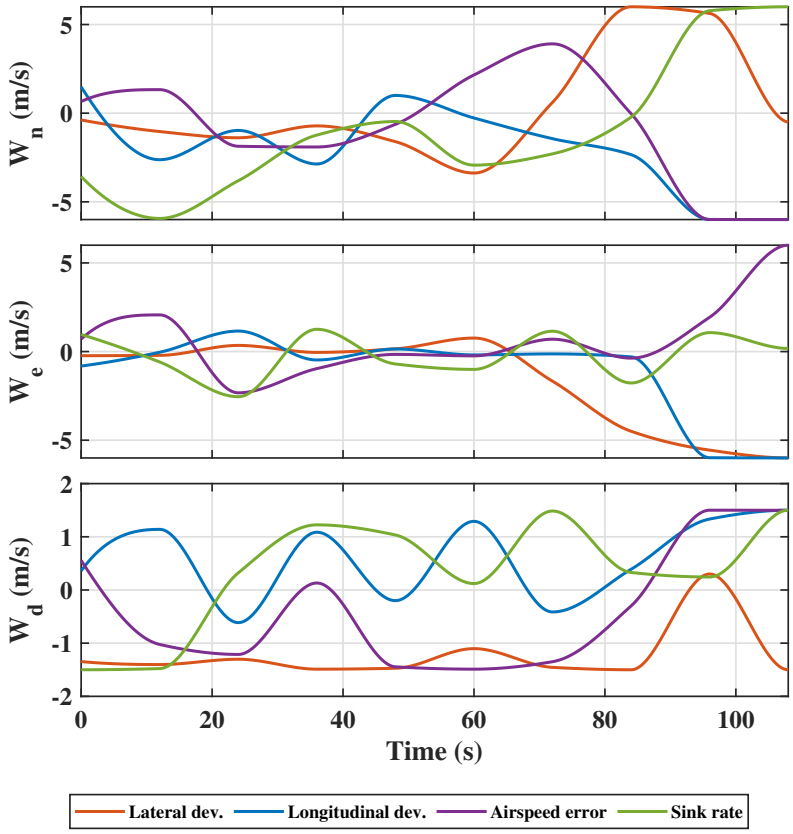


Fig. 5: Overlay of the four worst-case wind profiles.

influences the sink rate directly through vertical velocity kinematics. It affects the airspeed through lift and angle-of-attack perturbations. The sink-rate run produces $\dot{h}_{\mathrm{td}} = 1.60$ m/s. The optimizer employs a two-phase strategy comprising an initial updraft for $t < 72$ s and a subsequent 3 m/s transition to a terminal downdraft after $t > 84$ s. The lateral run, on the other hand,

Table 1: Landing performance under each worst-case wind. Bold entries are the targeted metrics.

Optimization target	Δy (m)	Δx (m)	ΔV_a (m/s)	$\dot{h}_{\mathrm{td}}$ (m/s)
Lateral Δy	**1.41**	34.93	0.92	0.44
Longitudinal Δx	0.06	**154.70**	1.95	1.24
Airspeed ΔV_a	0.21	154.64	**2.02**	1.23
Sink rate $\dot{h}_{\mathrm{td}}$	0.00	55.00	1.64	**1.60**

uses a sustained updraft. The airspeed run introduces a complex reversal in W_d. These distinct W_d profiles identify the unique physical coupling between vertical wind and each flight-performance metric.

Fig. 6 shows the spatial distribution of the wind for the sink-rate case. The wind vectors are small and point southward above 60 m. Below 40 m, the vectors grow and rotate northward. The headwind-to-tailwind reversal is visible along the trajectory. The color scale confirms that the horizontal wind speed exceeds 5 m/s only below 30 m. The disturbance is concentrated where the pitch and throttle authority is at its lowest.

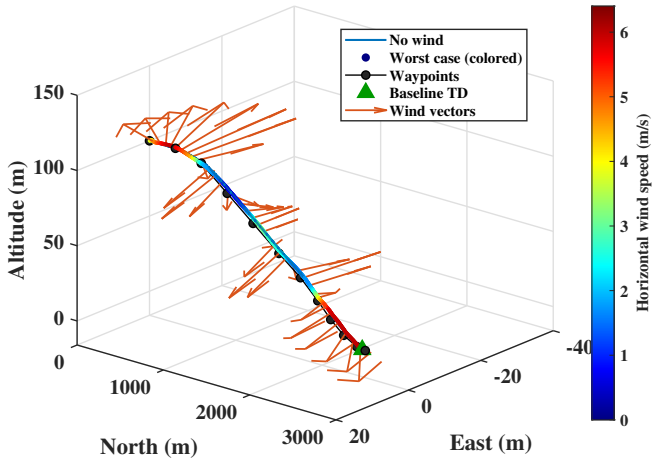


Fig. 6: Wind vectors along the flight trajectory for the sink-rate worst case.

5 Conclusion

This work applies counter optimization to identify worst-case wind disturbances during the landing of fixed-wing aircraft. For the designed closed-loop landing control system of fixed-wing aircraft, the physically constrained three-dimensional wind disturbance is treated as the decision variable in the counter optimization problem to maximize four core error metrics that indicate landing safety. They include maximization of lateral deviation, longitudinal deviation, airspeed error, and touchdown sink rate. The PSO algorithm is used to solve the optimization problem, thereby obtaining the worst-case disturbance sequences corresponding to the four indicators. The solution of this problem identifies the worst-case wind profile and the corresponding performance limit of the landing system.

References

1. Boeing Commercial Airplanes: Statistical Summary of Commercial Jet Airplane Accidents, Worldwide Operations 1959–2023. Boeing, Seattle, WA (2024). https://www.boeing.com/content/dam/boeing/boeingdotcom/company/about_bca/pdf/statsum.pdf
2. Beard, R.W., McLain, T.W.: Small Unmanned Aircraft: Theory and Practice. Princeton University Press, Princeton, NJ (2012)
3. Chen, W.-H., Yang, J., Guo, L., Li, S.: Disturbance-observer-based control and related methods: an overview. IEEE Trans. Ind. Electron. **63**(2), 1083–1095 (2016)
4. Lungu, M.: Backstepping and dynamic inversion control techniques for automatic landing of fixed wing unmanned aerial vehicles. Aerosp. Sci. Technol. **120**, Art. no. 107261 (2022)
5. Smeur, E.J.J., Chu, Q., de Croon, G.C.H.E.: Adaptive incremental nonlinear dynamic inversion for attitude control of micro air vehicles. J. Guid. Control Dyn. **39**(3), 450–461 (2016)
6. Wang, X., van Kampen, E.-J., Chu, Q.: Incremental sliding-mode fault-tolerant flight control. J. Guid. Control Dyn. **42**(2), 244–259 (2019)
7. Lu, H., Gao, L., Yan, Y., Hou, M., Wang, C.: Wind disturbance compensated path-following control for fixed-wing UAVs in arbitrarily strong winds. Chin. J. Aeronaut. **37**(2), 431–445 (2024)
8. Sun, Z., Wu, L., You, Y.: Automatic landing system design for unmanned fixed-wing vehicles via multivariable active disturbance rejection control. Int. J. Aerosp. Eng. **2023**, Art. no. 9395447 (2023)
9. Yin, M., Chu, Q.P., Zhang, Y., Niestroy, M.A., de Visser, C.C.: Probabilistic flight envelope estimation with application to unstable overactuated aircraft. J. Guid. Control Dyn. **42**(12), 2650–2663 (2019)
10. Lu, Z., Hong, H., Gerdts, M., Holzapfel, F.: Flight envelope prediction via optimal control-based reachability analysis. J. Guid. Control Dyn. **45**(1), 185–195 (2022)
11. Varga, A., Hansson, A., Puyou, G. (eds.): Optimization Based Clearance of Flight Control Laws: A Civil Aircraft Application. Lecture Notes in Control and Information Sciences, vol. 416. Springer, Berlin (2012)
12. Diepolder, J.: Optimal Control Based Clearance of Flight Control Laws. Ph.D. dissertation, Technical University of Munich (2021)
13. Braun, D., Schwaiger, F., Holzapfel, F., Diepolder, J., Ben-Asher, J.Z.: COLIBRY: a counter optimization library for MATLAB. In: AIAA Scitech 2023 Forum, AIAA Paper 2023-2584 (2023)
14. Braun, D., Marb, M.M., Angelov, J., Wechner, M., Holzapfel, F.: Worst-case analysis of complex nonlinear flight control designs using deep Q-learning. J. Guid. Control Dyn. **46**(7), 1365–1377 (2023)
15. Braun, D., Steffensen, R., Steinert, A., Holzapfel, F.: Counter optimization-based testing of flight envelope protections in a fly-by-wire control law using deep Q-learning. In: CEAS EuroGNC 2022, Paper CEAS-GNC-2022-076, Berlin (2022)
16. Braun, D., Holzapfel, F., Piprek, P., Schwalb, D.: Reinforcement learning-based flight control law clearance considering multiple complex constraints. In: AIAA Scitech 2025 Forum, AIAA Paper 2025-2809 (2025)